Chiral spin liquids at finite temperature in a three-dimensional Kitaev model

Yasuyuki Kato,[1] Yoshitomo Kamiya,[2] Joji Nasu,[3] and Yukitoshi Motome[1]
[1]*Department of Applied Physics, University of Tokyo, Hongo, 7-3-1, Bunkyo, Tokyo 113-8656, Japan*
[2]*Condensed Matter Theory Laboratory, RIKEN, Wako, Saitama 351-0198, Japan*
[3]*Department of Physics, Tokyo Institute of Technology, Meguro, Tokyo 152-8551, Japan*
(Received 18 July 2017; revised manuscript received 18 October 2017; published 7 November 2017)

Chiral spin liquids (CSLs) in three dimensions and thermal phase transitions to paramagnet are studied by unbiased Monte Carlo simulations. For an extension of the Kitaev model to a three-dimensional tricoordinate network dubbed the hypernonagon lattice, we derive low-energy effective models in two different anisotropic limits. We show that the effective interactions between the emergent Z_2 degrees of freedom called fluxes are unfrustrated in one limit, while highly frustrated in the other. In both cases, we find a first-order phase transition to the CSL, where both time-reversal and parity symmetries are spontaneously broken. In the frustrated case, however, the CSL state is highly exotic—the flux configuration is subextensively degenerate while showing a directional order with broken C_3 rotational symmetry. Our results provide two contrasting archetypes of CSLs in three dimensions, both of which allow approximation-free simulation for investigating the thermodynamics.

DOI: 10.1103/PhysRevB.96.174409

I. INTRODUCTION

The quantum spin liquid (QSL) is a long-standing subject, investigated for more than 40 years [1]. Recently, it attracted renewed attention not merely within basic science [2,3] but also due to its relevance to quantum computations [4,5]. The chiral spin liquid (CSL), which is the subject of this paper, belongs to a special subgroup of QSLs with spontaneous breaking of time-reversal ($\mathcal{T}$) symmetry. It has been a key concept in condensed matter physics, e.g., the fractional quantum Hall effect [6], high-T_c superconductivity [7,8], frustrated quantum Heisenberg models [8–12], and braiding of anyonic elementary excitations in QSLs [13,14].

Recently, a new trend in the study of CSLs has been created by exactly soluble models in the ground state [13–17]. This trend was initiated by an intriguing suggestion by Kitaev [13]: On a tricoordinate network with odd-site loops, one can construct a model that realizes an exact CSL ground state. Indeed, a quantum spin model on a decorated honeycomb network, which has triangles in the lattice structure, was exactly shown to have the CSL ground state [14]; the CSL can be either topologically trivial or nontrivial depending on the exchange couplings, accommodating Abelian or non-Abelian anyonic excitations, respectively [14]. The nature of the finite-temperature (T) phase transitions to these topologically different CSLs was also elucidated by using a quantum Monte Carlo simulation [18].

Compared to these studies of CSLs in two dimensions (2D), much less is known in three dimensions (3D). Nevertheless, 3D CSLs are intriguing because of exotic excitations specific to 3D, such as anyonic loop excitations of emergent fluxes [19] and Weyl semimetallic excitations of Majorana fermions [20]. These possibilities make the study of 3D CSLs at finite T even more interesting, including transitions breaking parity ($\mathcal{P}$) symmetry as well as $\mathcal{T}$ symmetry. While looplike excitations in the 3D Kitaev models and other realizations of 3D Z_2 QSL are known to trigger a thermal second-order phase transition [21–25], rather than a crossover in the case of 2D Z_2 QSL [26], the transitions to 3D CSLs remain elusive thus far.

In this paper, we present unbiased numerical results for 3D CSLs and thermal phase transitions to paramagnet. We consider an extension of the Kitaev model [13] defined on a three-dimensional tricoordinate network labeled by (9,3)a in the classification of Wells [20,27], which we call the hypernonagon lattice because the elementary loop consists of nine bonds. We derive the low-energy effective models for two distinct anisotropic limits, which are described by interacting Z_2 fluxes. We find that the effective model in one limit has no frustration while that in the other limit is highly frustrated. Using Monte Carlo (MC) simulations, we show that both models undergo a first-order phase transition from high-T paramagnet to a low-T CSL, where both $\mathcal{T}$ and $\mathcal{P}$ symmetries are spontaneously broken. Interestingly, neither of the two cases yields a uniform flux configuration in the low-T CSL states unlike in the 2D case [14]. Of particular interest is the frustrated case: The CSL has subextensive accidental degeneracy in the flux configuration, while exhibiting a directional order with breaking of C_3 rotational symmetry in addition to $\mathcal{T}$ and $\mathcal{P}$ symmetries.

This paper is organized as follows. In Sec. II, we introduce the extended Kitaev model on the hypernonagon lattice and derive the low-energy effective Hamiltonians in two distinct anisotropic limits. We also describe the MC method for investigating the thermodynamic behavior of the two low-energy models. In Sec. III, we present the MC results of thermodynamic behaviors of the two models as well as the analysis of the ground state properties. Finally, Sec. IV is devoted to the summary.

II. MODELS AND METHOD

A. Kitaev model on the hypernonagon lattice

We consider a straightforward extension of the Kitaev model [13] on the hypernonagon lattice shown in Fig. 1(a). The most noteworthy characteristics of this lattice distinct from many other 3D tricoordinate lattices is that it has odd-site loops. Such odd-site loops accommodate emergent Z_2 fluxes that are odd under both $\mathcal{T}$ and $\mathcal{P}$ operations, and hence, the

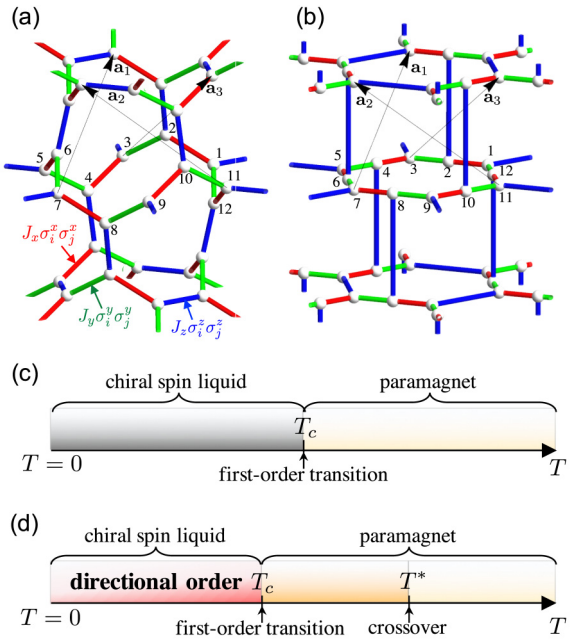

FIG. 1. (a) Hypernonagon-lattice Kitaev model and (b) the alternative visualization [20]. $\mathbf{a}_1$, $\mathbf{a}_2$, and $\mathbf{a}_3$ are the primitive vectors. The spheres represent the $S = 1/2$ spins. The sublattice indices for 12 spins in a unit cell are shown. Schematic finite-T phase diagrams in (c) the large J_z limit and (d) the large J_x limit.

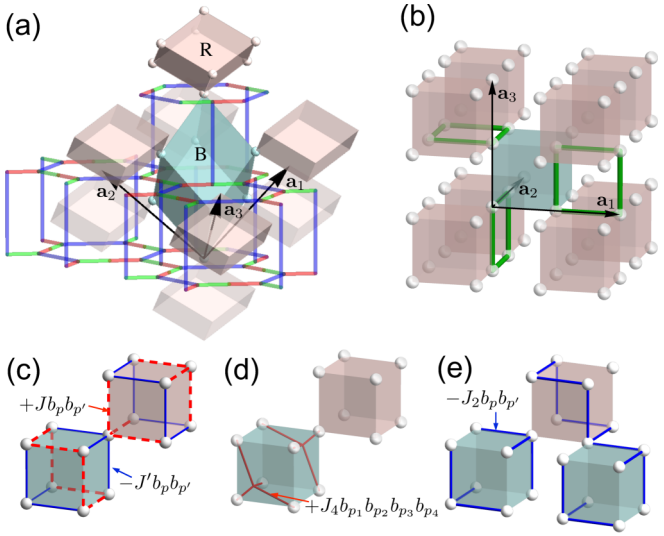

FIG. 2. Relation between the hypernonagon lattice and the lattice of b_p in the effective models in Eqs. (3) and (4). (a) A distorted cubic lattice where the spheres represent b_p. Each b_p is shared by the two different types of cubes, i.e., bluish (B) and redish (R) cubes that correspond to different types of closed volumes in the hypernonagon lattice. (b) A 3D checkerboard lattice topologically equivalent to (a). The green squares represent examples of the four-site loops of b_p for MC update. The interactions between b_p for (c) the large J_z limit and (d),(e) the large J_x limit.

ground state of the system can be a CSL [13]. The Hamiltonian of the hypernonagon Kitaev model is given by

$$\mathcal{H} = \sum_{\mu=\{x,y,z\}} \mathcal{H}_\mu, \quad \mathcal{H}_\mu = -J_\mu \sum_{\langle i,j\rangle_\mu} \sigma_i^\mu \sigma_j^\mu, \tag{1}$$

where σ_i^μ ($\mu = x,y,z$) is a Pauli matrix ($\sigma_i^z = \pm 1$) at site i and the sum $\sum_{\langle i,j\rangle_\mu}$ runs over all the nearest neighbors connected by μ bonds shown in Fig. 1(a) [see also Fig. 1(b)]. The number of elementary nine-site loops is eight per unit cell, and the centers of these loops can be combined into a "cube," as shown in Fig. 2(a). Each loop center is shared by the two different types of cubes, i.e., bluish (B) and redish (R) cubes in Fig. 2(a). These corner-sharing cubes form a 3D version of the checkerboard lattice as shown in Fig. 2(b).

For each nine-site loop, one can define the Z_2 flux operator

$$W_p = -i \prod_{\langle i,j\rangle_\mu \in p} \sigma_i^\mu \sigma_j^\mu, \tag{2}$$

where the product is taken for all the bonds in the loop p in a clockwise manner viewed from the center of each B cube [Fig. 2(a)]. W_p is a conserved quantity which is odd under both $\mathcal{T}$ and $\mathcal{P}$ operations with the eigenvalues ± 1 (called $\pm\pi/2$ flux [20]). Similar to other 3D cases [20,22], there are local constraints on W_p corresponding to the operator identities for Pauli matrices: The product of eight W_p is always unity in each B and R cube. Thus, the eigenstates of the model in Eq. (1) are divided into the sectors with different configurations of W_p, and hence, the ground state can be, in principle, obtained by comparing the eigenenergies. According to the variational calculation, however, the hypernonagon model has complexity: Low-energy sectors are nearly degenerate when $J_x \sim J_y \sim J_z$ [20].

B. Low-energy effective Hamiltonians in two anisotropic limits

We derive low-energy effective Hamiltonians of Eq. (1) in two different anisotropic limits: the large J_z limit ($J_z \gg J_x, J_y$) and the large J_x limit ($J_x \gg J_y, J_z$) [28]. Following the derivation of the toric code for the honeycomb Kitaev model [13], we perform the perturbation expansion in terms of $\mathcal{H} - \mathcal{H}_\mu$ for the unperturbed Hamiltonian $\mathcal{H}_\mu$. The effective Hamiltonians can be written in terms of Z_2 variables describing the flux states for each loop. By the expansion up to the eighth order, we obtain the following effective Hamiltonians, $\mathcal{H}^z_{\rm eff}$ and $\mathcal{H}^x_{\rm eff}$, for the large J_z and J_x limits, respectively:

$$\mathcal{H}^z_{\rm eff} = J \sum_{\langle p,p'\rangle} b_p b_{p'} - J' \sum_{(p,p')} b_p b_{p'}, \tag{3}$$

$$\mathcal{H}^x_{\rm eff} = J_4 \sum_{\langle p_1,p_2,p_3,p_4\rangle} b_{p_1} b_{p_2} b_{p_3} b_{p_4} - J_2 \sum_{(p,p')} b_p b_{p'}, \tag{4}$$

with

$$J = \frac{33}{2048} \frac{J_x^4 J_y^4}{|J_z^7|}, \quad J' = \frac{9}{33} J, \tag{5}$$

$$J_2 = \frac{9}{2048} \frac{J_y^4 J_z^4}{|J_x^7|}, \quad J_4 = \frac{63}{512} \frac{J_y^6}{|J_x^5|}. \tag{6}$$

J, J', and J_2 are obtained by the eighth-order perturbation, while J_4 is the sixth-order one [29]. See Appendix for details

of the derivation. Here, b_p is a Z_2 variable defined as

$$b_p = \mathcal{P}_\mu W_p \mathcal{P}_\mu = \pm 1, \tag{7}$$

where $\mathcal{P}_\mu$ is the projection to the ground state manifold of $\mathcal{H}_\mu$. The models include no odd-order term in b_p, precluded by $\mathcal{T}$ and $\mathcal{P}$ symmetries. The sums $\sum_{\langle p,p'\rangle}$ and $\sum_{(p,p')}$ run over the specific bonds indicated by solid blue and dashed red lines, respectively, in Figs. 2(c) and 2(e), while $\sum_{\langle p_1,p_2,p_3,p_4\rangle}$ runs over "clusters" comprising four b_p as shown in Fig. 2(d). Similar to W_p, b_p obeys the local constraints, i.e., the product of eight b_p in each cube must be unity. In addition, there are two global constraints, similar to the hyperhoneycomb case [22,30].

C. Monte Carlo method

As both $\mathcal{H}^z_{\rm eff}$ and $\mathcal{H}^x_{\rm eff}$ are given in terms of the static Z_2 variables b_p, their thermodynamic properties can be investigated by classical MC simulations, similar to Ref. [23]. To satisfy the local and global constraints discussed above, a pair of four-site loops of b_p must be flipped simultaneously in a single update in the MC simulation [30]. Examples of the four-site loops are shown in Fig. 2(b). We adopt the annealing technique unless otherwise noted. The observables and statistical errors are evaluated from 24–384 independent sets of 10^5-10^7 MC samples.

III. RESULTS

In this section, we present the results of analysis of the low-energy effective Hamiltonians on their ground states and thermodynamic behaviors for both the large J_z and large J_x limits.

A. Large J_z limit

1. Ground state

Let us first discuss the effective model in the large J_z limit, $\mathcal{H}^z_{\rm eff}$ in Eq. (3). The model has no frustration in J and J', and hence, the lowest-energy state is given by a staggered-type order of b_p in the [111] direction; see the inset of Fig. 3(b). This coincides with the 0-flux state, for which Weyl semimetallic excitations are expected when the system is gapless [20].

Since the effective model in Eq. (3) is unfrustrated, all the bonds can optimize the interaction energies. Hence the ground state energy per b_p is simply computed as

$$\varepsilon^z_{\rm GS} = -\frac{3J+3J'}{2} = -\frac{21}{11}J. \tag{8}$$

2. Monte Carlo simulation at finite temperature

Figure 3 shows the MC results for the large J_z model. We find that the system undergoes a phase transition at $T_c \simeq 3J$ with a discontinuous jump in the energy density $\varepsilon^z \equiv \langle \mathcal{H}^z_{\rm eff}\rangle / N_{b_p}$ ($N_{b_p} = 8L^3$ is the number of b_p sites and L is the linear dimension of the b_p lattice in Fig. 2). Below T_c, the staggered flux order parameter, defined as $\sqrt{\langle \mathcal{B}^2\rangle}/N_{b_p}$ where $\mathcal{B} = \sum_p (-1)^p b_p$, becomes nonzero with a jump from 0 to $\approx$1 in the thermodynamic limit. These observations indicate that the system undergoes a strong first-order transition from the paramagnetic phase to the CSL phase [Fig. 1(c)].

Regarding this discontinuous behavior, both the constraints on b_p and the peculiar symmetry of b_p defined on odd-site loops must play a central role. Without the constraints, $\mathcal{H}^z_{\rm eff}$ is merely an unfrustrated Ising model, which undergoes a continuous transition. Similarly, when the system is composed of even-site loops, the leading term in perturbation theory is linear in the flux variable, which can also be mapped onto an unfrustrated Ising model by a duality transformation [23,25].

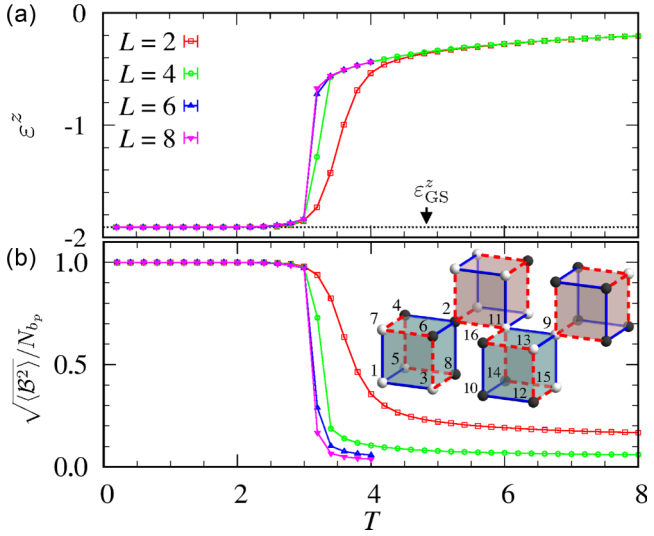

FIG. 3. Temperature dependence of (a) the energy density ε^z and (b) the order parameter $\sqrt{\langle \mathcal{B}^2\rangle}/N_{b_p}$ for the large-J_z effective model $\mathcal{H}^z_{\rm eff}$ in Eq. (3). We set $J = 1$ ($J' = 9/33$). $\varepsilon^z_{\rm GS}$ indicates the ground state energy in Eq. (8) for the b_p configuration in the inset of (b); the black (white) spheres represent $b_p = -1(+1)$ [or $b_p = +1(-1)$], and the numbers denote the sublattices.

B. Large J_x limit

1. Ground state

Next we discuss the effective model in the large J_x limit, $\mathcal{H}^x_{\rm eff}$ in Eq. (4). In contrast to the large J_z model $\mathcal{H}^z_{\rm eff}$, the model suffers from frustration, and the ground state manifold exhibits substantial degeneracy for $J_4 \gg J_2$ (note that J_4 is in the lower-order perturbation than J_2). First of all, the four-body interactions in the J_4 terms must be optimized: $b_{p_1}b_{p_2}b_{p_3}b_{p_4} = -1$ in every four-flux cluster $\langle p_1,p_2,p_3,p_4\rangle$ shown in Fig. 2(d). Any of the resulting configurations corresponds to a π-flux state, in contrast to the 0-flux state in the large J_z limit [20]. In addition to this condition, the ground state manifold satisfies the following three energetics (i)–(iii). First, (i) J_2 favors six configurations in each four-flux cluster shown in Fig. 4(a); here we note that the π-flux states cannot optimize all the J_2 terms simultaneously. Also note that the local constraint associated with a given B cube is fulfilled for any combination of the six states for a pair of four-b_p clusters per B cube. Meanwhile, (ii) the six-site network of J_2 within each R cube [Fig. 2(e)] favors six b_p on the buckled hexagon (h) to be either all $+1$ or all -1. Finally, the energetics (ii) also implies that (iii) the two remaining b_p on each R cube, i.e., not on the hexagon h, [for example p_a and p_b in the inset of Fig. 6(a)] must take the same value because of the local constraint on R cubes.

On the basis of the consideration above, we obtain the ground state energy of the effective model in Eq. (4) as follows.

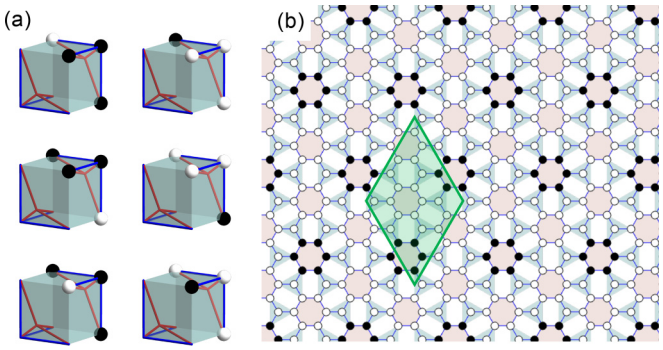

FIG. 4. (a) Six configurations in a four-flux cluster minimizing its intracluster interaction energy (J_4 and J_2 interaction). (b) An example of the b_p configurations in the ground state manifold on a (111) hexagon-triangular plane in the large J_x limit. The rhombic region indicated by the green solid line is the unit cell.

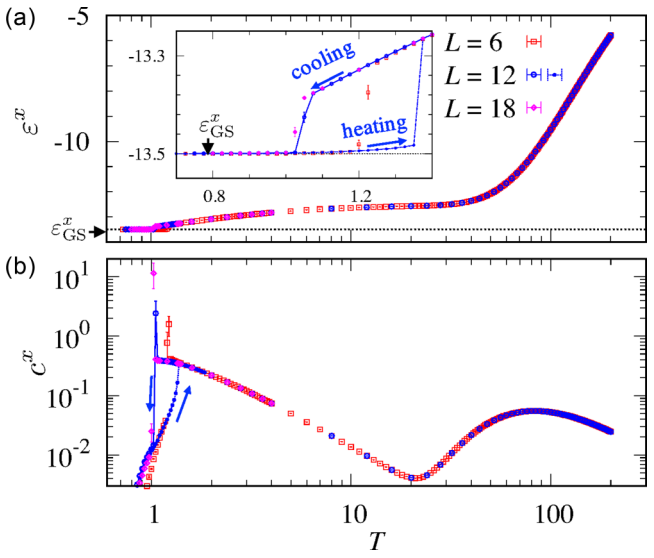

FIG. 5. Temperature dependence of (a) the energy density ε^x and (b) the specific heat c^x for the large-J_x effective model $\mathcal{H}^x_{\rm eff}$ in Eq. (4). We set $J_2 = 1$ and $J_4 = 50$. $\varepsilon^x_{\rm GS}$ indicates the ground state energy in Eq. (9). The inset of (a) shows an enlarged view of the main panel. The data of cooling and heating processes are for demonstrating the hysteresis (the heating process is shown only for $L = 12$).

The largest contribution to the ground state energy is $-J_4$ per 4 b_p, i.e., $-J_4/4$ per b_p, from the J_4 terms. To count the energy contribution from the J_2 term, let us consider an example of the b_p configurations which satisfy the energetics (i)–(iii). For this purpose, it is convenient to view the 3D checkerboard lattice from the [111] direction, and to extract a layer of b_p connected by the J_2 bonds; the system can be regarded as a stacking of "hexagon-triangular" layers, as shown in Fig. 4(b). The black and white circles in Fig. 4(b) exemplifies a ground state configuration in a (111) hexagon-triangular plane, whose unit cell is relatively small (including 24 b_p and 36 J_2 bonds, as shown by the green rhombus). The two-body interactions in the J_2 term are satisfied on the 30 bonds, while unsatisfied on the 6 bonds. Thus, the energy contribution from the J_2 term is $(6-30)J_2 = -24J_2$ per unit cell, i.e., $-J_2$ per b_p. The ground state b_p configurations must satisfy also the energetics (iii) arising from the local constraint. This is readily satisfied by stacking the optimized b_p configurations like in Fig. 4 in a proper manner. Thus, we find the ground state energy per b_p in the large J_x limit as

$$\varepsilon^x_{\rm GS} = -J_2 - \frac{J_4}{4}. \tag{9}$$

2. *Monte Carlo simulation at finite temperature*

Figure 5 shows the MC results for $\mathcal{H}^x_{\rm eff}$, where we set $J_2/J_4 = 0.02$ considering that J_2 is higher order in perturbation theory than J_4. While decreasing T, there are two successive drops in $\varepsilon^x = \langle \mathcal{H}^x_{\rm eff}\rangle / N_{b_p}$ at $T^* \sim J_4$ and $T_c \sim J_2$. Correspondingly, the specific heat $c^x = \partial \varepsilon^x / \partial T$ exhibits a broad peak at T^* and a sharp peak at T_c. T^* is a crossover temperature, below which configurations with $b_{p_1} b_{p_2} b_{p_3} b_{p_4} = 1$ is exponentially suppressed in every four-flux cluster $\langle p_1, p_2, p_3, p_4\rangle$ shown in Fig. 2(d). Upon further decreasing T, the three local energetics (i)–(iii) discussed above emerge.

In fact, the singularity at T_c signals a transition to a CSL state in which the above (i)–(iii) are all satisfied in the $T = 0$ limit. As evidenced by the hystereses in ε^x and c^x in Fig. 5, this transition is also of first order.

As discussed in Sec. III B 1, the energetics (i)–(iii) cannot select out an ordered configuration of b_p, and leave subextensive degeneracy. In the MC simulation below T_c, we also find the subextensive degeneracy in the b_p configurations, along with spontaneous breaking of a point-group symmetry below T_c. To explain this, we show a MC snapshot on a (111) hexagon-triangular plane in Fig. 6(a). Here, the hexagons are the J_2 networks in each R cube, in most of which $B_h \equiv \sum_{p\in h} b_p/6 = \pm 1$ below T_c because of the energetics (ii). In a given hexagon-triangular layer, three buckled hexagons, say h_1, h_2, and h_3 forming a triangle, are interconnected by a four-flux J_4 cluster in a B cube [see the inset of Fig. 6(a)]. Because of the frustrated energetics (i), the ground state has $B_{h_1} B_{h_2} B_{h_3} = -1$ for any triangle, resembling the situation in the triangular-lattice Ising model [31]. However, unlike this classic problem, the flux configurations generated by MC simulation appear to break C_3 rotational symmetry; an example is shown in Fig. 6(a). We confirm the C_3 breaking by measuring the bond order parameter with respect to B_h defined as follows. At first, we consider a direction specific correlator of B_h as

$$r_\nu \equiv \frac{1}{N_h} \sum_h B_h B_{h+\mathbf{d}_\nu}, \tag{10}$$

where $\mathbf{d}_\nu$ ($\nu = 1,2,3$) are the inplane vectors shown in Fig. 6(a), the sum $\sum_h$ runs over all the hexagons h in every second (111) layers (hexagon-triangular layers) connected by the effective interaction, and N_h is the number of the hexagons. Then, we define the bond order parameter as

$$\frac{1}{2}\left(3r_{\rm max} - \sum_{\nu=1}^{3} \langle r_\nu \rangle\right), \tag{11}$$

where $r_{\rm max} = \langle \max[r_1, r_2, r_3]\rangle$. As plotted in Fig. 6(b), the bond order parameter becomes finite below T_c, which is

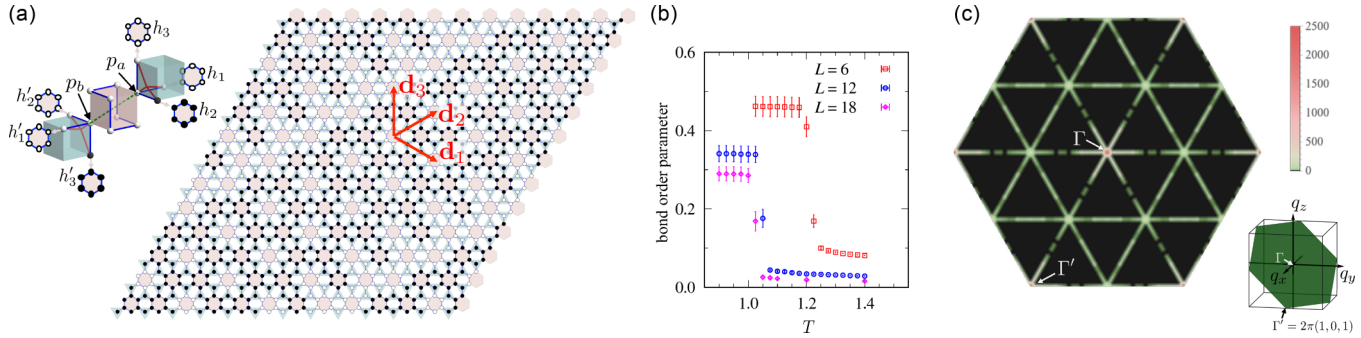

FIG. 6. (a) MC snapshot of the b_p configurations below T_c on a hexagon-triangular layer corresponding to a (111) slice of the 3D checkerboard lattice in Fig. 2. The black (white) circles represent $b_p = -1(+1)$. The inset illustrates an example of a favored configuration for a pair of four-b_p J_4 clusters on the second adjacent (111) hexagon-triangular layers at low T. (b) Temperature dependence of the bond order parameter with respect to B_h defined in Eq. (11). (c) Structure factor for b_p on the plane of $q_x + q_y + q_z = 0$ (see the inset). The data are obtained below T_c by averaging over ~300 MC samples for $L = 18$.

an indication of the directional order selecting one of three directions $\mathbf{d}_v$ shown in Fig. 6(a). Likewise, in the structure factor

$$S(\mathbf{q}) \equiv \frac{1}{N_{b_p}} \langle b_{\mathbf{q}} b_{-\mathbf{q}} \rangle, \tag{12}$$

with $b_{\mathbf{q}} = \sum_p b_p e^{-i\mathbf{q}\cdot\mathbf{r}_p}$ ($\mathbf{r}_p$ is the position vector for the site p), we find diffusive lines in $S(\mathbf{q})$ consistent with the directional order.

This "locking transition" is suggested to be induced by the interlayer coupling, similar to the Ising model on the stacked triangular layers [32–38]. Coming back to the consideration of the energetics (iii), the two b_p in a R cube not included in a buckled hexagon [b_{p_a} and b_{p_b} in the inset of Fig. 6(a)] also belong to four-flux J_4 clusters that are on second adjacent layers. As each of them combines three buckled hexagons (say, $h_1 - h_3$ and $h'_1 - h'_3$) on each (111) honeycomb-triangular layer, the energetics (iii) implies an effective interlayer coupling favoring $(B_{h_1} + B_{h_2} + B_{h_3})(B_{h'_1} + B_{h'_2} + B_{h'_3}) = +1$. This is expected to play an important role in the locking transition; in fact, $S(\mathbf{q} = 0)$ is divergent below T_c. This is also an indication of breaking of $\mathcal{T}$ and $\mathcal{P}$ symmetries in the low-T CSL.

Thus, in the large J_x limit, the system exhibits a first-order transition similar to the large J_z limit, but the low-T CSL state is not completely ordered while it has the directional order with the uniform component of b_p [Fig. 1(d)]. The CSL phase is highly unusual—it is not ordered in the double meaning: The original spins σ_i in Eq. (1) are disordered, and in addition, the emergent Z_2 fluxes b_p are not completely ordered. However, it is characterized by a directional order with broken C_3 rotational symmetry. The peculiar nature may yield more exotic elementary excitations than ever studied in 3D CSLs.

IV. SUMMARY

In summary, we discovered two distinct 3D CSLs, both of which allow unbiased simulations for the thermodynamics. We showed that one of them suffers from severe frustration in interacting Z_2 fluxes. By unbiased Monte Carlo simulations, we found that both CSLs undergo a first-order phase transition to paramagnet. Remarkably, the frustrated CSL retains degeneracy while showing a directional order. Our discovery of two interesting cases will stimulate further studies of 3D CSLs. Nature of elementary excitations will be an intriguing future issue, especially for the exotic directionally-ordered CSL.

ACKNOWLEDGMENTS

The authors thank S. Trebst and M. Hermanns for stimulating discussion in the early stage of this study. This work was supported by JSPS Grant No. 26800199, No. JP15K13533, No. JP16K17747, No. JP16H02206, and No. JP16H00987. Numerical calculations were conducted on the supercomputer system in ISSP, The University of Tokyo.

APPENDIX: DERIVATION OF THE LOW-ENERGY EFFECTIVE HAMILTONIAN

In this Appendix, we show how to derive the low-energy effective Hamiltonians in Eqs. (3) and (4). We derive the effective Hamiltonians from the Kitaev model on the hyper-nonagon lattice in Eq. (1) for the large J_z and large J_x limits, by following the way to derive the toric code in the anisotropic limit of the original Kitaev model on a honeycomb lattice [13]. In the large J_μ limit ($\mu = z$ or x), we regard $\mathcal{H}_0 = \mathcal{H}_\mu$ and the rest $\mathcal{H}_1 = \mathcal{H} - \mathcal{H}_0$ as an unperturbed Hamiltonian and a perturbation, respectively. The unperturbed states for $\mathcal{H}_0$ are composed of the independent dimers on the μ bonds. Each dimer is described by a new spin 1/2 degree of freedom $\boldsymbol{\tau}$, and the ground state for $\mathcal{H}_0$ is given by a direct product of the states $|\tau^z_{ij} = \pm 1\rangle = |\sigma^\mu_i = \mathrm{sgn}(J_\mu)\sigma^\mu_j = \pm 1\rangle$ for all the μ bonds ($\langle i,j\rangle_\mu$). When we define $\boldsymbol{\tau}$ at the center of each μ bond, the lattice structure for the $\boldsymbol{\tau}$ degree of freedom looks like Figs. 7(c) and 7(d) for the large J_z and J_x limits, respectively: The blue z (red x) bonds in Figs. 7(a) and 7(b) are replaced by the blue (red) sites. The former is regarded as a layered Lieb lattice, while the latter a layered honeycomb lattice.

When we introduce $\mathcal{H}_1$ as the perturbation, the nth-order contribution to the low-energy effective Hamiltonian is

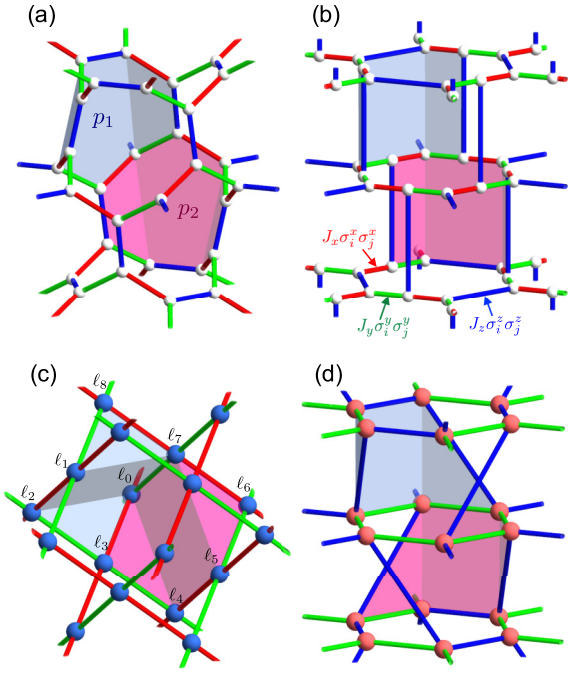

FIG. 7. (a),(b) The hypernonagon lattice reproduced from Figs. 1(a) and 1(b). The blue and red plaquettes represent a neighboring pair of the nine-site loops (p_1 and p_2), on which the local conserved quantities W_p are defined. (c) A layered Lieb lattice [(d) a layered honeycomb lattice] obtained by contracting all the z bonds (x bonds) for the large J_z (J_x) limit. The blue and red plaquettes represent b_{p_1} and b_{p_2}, respectively. The reddish and bluish spheres represent the sites where the τ degree of freedom in the low-energy effective models is defined.

given by

$$\mathcal{H}_\mu^{(n)} = \mathcal{P}_\mu[(\mathcal{H}_1\mathcal{S})^{n-1}\mathcal{H}_1]\mathcal{P}_\mu^\dagger, \tag{A1}$$

where $\mathcal{P}_\mu$ is the projection to the low-energy subspace spanned by the direct product of the states $|\tau_{ij}^z = \pm 1\rangle$;

$$\mathcal{S} \equiv \frac{1-\mathcal{P}_\mu^\dagger\mathcal{P}_\mu}{E_0-\mathcal{H}_0}, \tag{A2}$$

where E_0 is the ground state energy of $\mathcal{H}_0$. The effective Hamiltonians in Eqs. (3) and (4) are obtained by using Eq. (A1) up to the eighth-order perturbation. We note that Eq. (A1) is not generic but valid for sufficiently low orders of the expansion. For example, the generic form for the fourth-order contributions is obtained as [39]

$$\mathcal{P}_\mu[(\mathcal{H}_1\mathcal{S})^3\mathcal{H}_1]\mathcal{P}_\mu^\dagger - \tfrac{1}{2}[\mathcal{P}_\mu\mathcal{H}_1\mathcal{S}^2\mathcal{H}_1\mathcal{P}_\mu^\dagger\mathcal{P}_\mu\mathcal{H}_1\mathcal{S}\mathcal{H}_1\mathcal{P}_\mu^\dagger + \mathcal{P}_\mu\mathcal{H}_1\mathcal{S}\mathcal{H}_1\mathcal{P}_\mu^\dagger\mathcal{P}_\mu\mathcal{H}_1\mathcal{S}^2\mathcal{H}_1\mathcal{P}_\mu^\dagger]. \tag{A3}$$

The second term in Eq. (A3) is omitted in Eq. (A1). Since the nth-order perturbation lower than or equal to the eighth order in the large J_z case (the sixth order in the large J_x case) leads to only constants, we neglect the contributions from the second term in Eq. (A3) in the following calculations.

The derivation of the effective models in Eqs. (3) and (4) is lengthy but straightforward. For instance, let us consider the two-body J term in Eq. (3). It is derived from the eight-site loop ℓ_1-ℓ_2-$\cdots$-ℓ_8 in Fig. 7(c). The eight-site loop is made of two neighboring six-site elementary loops p_1 (blue plaquette ℓ_8-ℓ_7-ℓ_0-ℓ_3-ℓ_2-ℓ_1) and p_2 (red plaquette ℓ_4-ℓ_3-ℓ_0-ℓ_7-ℓ_6-ℓ_5), as shown in Fig. 7(c). By the perturbation on this eight-site loop [eighth-order perturbation in $\mathcal{H}_1$ by using Eq. (A1)], we obtain

$$-J\tau_{\ell_1}^y\tau_{\ell_2}^z\tau_{\ell_3}^x\tau_{\ell_4}^y\tau_{\ell_5}^y\tau_{\ell_6}^z\tau_{\ell_7}^x\tau_{\ell_8}^y. \tag{A4}$$

The blue and red plaquettes are originally derived from those in Figs. 7(a) and 7(b), on which the Z_2 conserved quantities W_p are defined. Hence, we can rewrite Eq. (A4) by using the Z_2 variables b_p which are defined as the projection of W_p [Eq. (7)]. For the blue and red plaquettes, b_p are given as

$$b_{p_1} = \tau_{\ell_8}^y\tau_{\ell_7}^y\tau_{\ell_0}^z\tau_{\ell_3}^z\tau_{\ell_2}^z\tau_{\ell_1}^y, \tag{A5}$$

$$b_{p_2} = -\tau_{\ell_4}^y\tau_{\ell_3}^y\tau_{\ell_0}^z\tau_{\ell_7}^z\tau_{\ell_6}^z\tau_{\ell_5}^y. \tag{A6}$$

Thus, the eighth-order perturbation term in Eq. (A4) is rewritten into the two-body interaction $Jb_{p_1}b_{p_2}$. The other interaction terms in Eqs. (3) and (4) can be derived in a similar manner. We note that the combination of b_{p_1} and b_{p_2} in the large J_x limit corresponds to a ten-site loop as shown in Fig. 7(d), and thus there is no interaction between p_1 and p_2 in Eq. (4) within the eighth-order perturbation.

[1] P. Anderson, Mater. Res. Bull. **8**, 153 (1973).
[2] L. Balents, Nature (London) **464**, 199 (2010).
[3] C. Lacroix, P. Mendels, and F. Mila, *Introduction to Frustrated Magnetism: Materials, Experiments, Theory* (Springer, Berlin, Heidelberg, 2011).
[4] A. Kitaev, Ann. Phys. **303**, 2 (2003).
[5] C. Nayak, S. H. Simon, A. Stern, M. Freedman, and S. Das Sarma, Rev. Mod. Phys. **80**, 1083 (2008).
[6] R. B. Laughlin and Z. Zou, Phys. Rev. B **41**, 664 (1990).
[7] P. W. Anderson, Science **235**, 1196 (1987).
[8] X.-G. Wen, F. Wilczek, and A. Zee, Phys. Rev. B **39**, 11413 (1989).
[9] V. Kalmeyer and R. B. Laughlin, Phys. Rev. Lett. **59**, 2095 (1987).
[10] L. Messio, B. Bernu, and C. Lhuillier, Phys. Rev. Lett. **108**, 207204 (2012).
[11] B. Bauer, L. Cincio, B. Keller, M. Dolfi, G. Vidal, S. Trebst, and A. Ludwig, Nat. Commun. **5**, 5137 (2014).
[12] S.-S. Gong, W. Zhu, and D. Sheng, Sci. Rep. **4**, 6317 (2014).
[13] A. Kitaev, Ann. Phys. **321**, 2 (2006).
[14] H. Yao and S. A. Kivelson, Phys. Rev. Lett. **99**, 247203 (2007).
[15] D. F. Schroeter, E. Kapit, R. Thomale, and M. Greiter, Phys. Rev. Lett. **99**, 097202 (2007).
[16] M. Hermanns, I. Kimchi, and J. Knolle, Annu. Rev. Condens. Matter Phys. **9**, 17 (2018).
[17] S. Dusuel, K. P. Schmidt, J. Vidal, and R. L. Zaffino, Phys. Rev. B **78**, 125102 (2008).
[18] J. Nasu and Y. Motome, Phys. Rev. Lett. **115**, 087203 (2015).

[19] T. Si and Y. Yu, Nucl. Phys. B **803**, 428 (2008).
[20] K. O'Brien, M. Hermanns, and S. Trebst, Phys. Rev. B **93**, 085101 (2016).
[21] C. Castelnovo and C. Chamon, Phys. Rev. B **78**, 155120 (2008).
[22] S. Mandal and N. Surendran, Phys. Rev. B **90**, 104424 (2014).
[23] J. Nasu, T. Kaji, K. Matsuura, M. Udagawa, and Y. Motome, Phys. Rev. B **89**, 115125 (2014).
[24] J. Nasu, M. Udagawa, and Y. Motome, Phys. Rev. Lett. **113**, 197205 (2014).
[25] Y. Kamiya, Y. Kato, J. Nasu, and Y. Motome, Phys. Rev. B **92**, 100403 (2015).
[26] J. Nasu, M. Udagawa, and Y. Motome, Phys. Rev. B **92**, 115122 (2015).
[27] A. F. Wells, *Three Dimensional Nets and Polyhedra* (Wiley, New York, 1977).
[28] The large J_y limit is equivalent to the large J_x limit by symmetry.
[29] For J_4, we only consider the leading contribution.
[30] Y. Kato, Y. Kamiya, J. Nasu, and Y. Motome, Physica B, doi: 10.1016/j.physb.2017.08.008.
[31] G. H. Wannier, Phys. Rev. **79**, 357 (1950).
[32] D. Blankschtein, M. Ma, A. N. Berker, G. S. Grest, and C. M. Soukoulis, Phys. Rev. B **29**, 5250 (1984).
[33] S. N. Coppersmith, Phys. Rev. B **32**, 1584 (1985).
[34] F. Matsubara and S. Inawashiro, J. Phys. Soc. Jpn. **56**, 2666 (1987).
[35] R. Moessner, S. L. Sondhi, and P. Chandra, Phys. Rev. Lett. **84**, 4457 (2000).
[36] S. V. Isakov and R. Moessner, Phys. Rev. B **68**, 104409 (2003).
[37] Y. Jiang and T. Emig, Phys. Rev. Lett. **94**, 110604 (2005).
[38] S.-Z. Lin, Y. Kamiya, G.-W. Chern, and C. D. Batista, Phys. Rev. Lett. **112**, 155702 (2014).
[39] M. Takahashi, J. Phys. C: Solid State Phys. **10**, 1289 (1977).